Fe-facilitated dynamic active site generation on spinel CoAl₂O₄ with self-termination of surface reconstruction for water oxidation

Tianze Wu[1,2,Δ], Shengnan Sun[1,2,Δ], Jiajia Song[1,Δ], Shibo Xi[3], Yonghua Du[3], Bo Chen[1], Wardhana Aji Sasangka[4], Hanbin Liao[1,5], Chee Lip Gan[1,4], Günther G. Scherer[6,7], Lin Zeng[8], Haijiang Wang[8], Hui Li[9], Alexis Grimaud[10,11]* and Zhichuan J. Xu[1,2,12] *

[1]School of Materials Science and Engineering, Nanyang Technological University, 50 Nanyang Avenue, 639798, Singapore;

[2]Solar Fuels Laboratory and Energy Research Institute, Nanyang Technological University, 50 Nanyang Avenue, 639798, Singapore;

[3]Institute of Chemical and Engineering Sciences A*STAR, 1 Pesek Road, 627833, Singapore;

[4]Low Energy Electronic Systems, Singapore-MIT Alliance for Research and Technology, Singapore 138602, Singapore;

[5]Nanyang Environment and Water Research Institute (NEWRI), Interdisciplinary Graduate School (IGS), Nanyang Technological University, 1 Cleantech Loop, CleanTech One, 637141, Singapore;

[6]Department for Management of Science and Technology Development, Ton Duc Thang University, Ho Chi Minh City, Vietnam;

[7]Faculty of Applied Sciences, Ton Duc Thang University, Ho Chi Minh City, Vietnam;

[8]Department of Mechanical and Energy Engineering, Southern University of Science and Technology, Shenzhen, 518055, Guangdong, China;

[9]Department of Materials Science and Engineering, Southern University of Science and Technology, Shenzhen 518055, Guangdong, China;

[10]Chimie du Solide et de l'Energie, UMR 8260, Collège de France, 75231 Paris Cedex 05, France;

[11]Réseau sur le Stockage Electrochimique de l'Energie (RS2E), CNRS FR 3459,33 rue Saint Leu, 80039, Amiens Cedex, France;

[12]Energy Research Institute @ Nanyang Technological University, 50 Nanyang Avenue, Singapore 639798, Singapore.

△These authors contribute equally to this work.

*e-mail: xuzc@ntu.edu.sg; alexis.grimaud@college-de-france.fr.

Abstract

The development of efficient and low-cost electrocatalysts for oxygen evolution reaction is critical for improving the water electrolysis efficiency. Here we report a strategy using Fe substitution to enable the inactive spinel $CoAl_2O_4$ to become highly active and superior to the benchmark IrO_2. The Fe substitution is revealed to facilitate the surface reconstruction into active Co oxyhydroxides under OER conditions. It also activates the deprotonation on the reconstructed oxyhydroxide to induce negatively charged oxygen as active site, thus significantly enhancing the OER activity of $CoAl_2O_4$. Furthermore, it promotes the pre-oxidation of Co and introduces great structural flexibility due to the uplift of the O 2p levels. This results in an accumulation of surface oxygen vacancy along with lattice oxygen oxidation that terminates as Al^{3+} leaches, preventing further reconstruction. We showcase a promising way to achieve tunable electrochemical reconstruction by optimizing the electronic structure for low-cost and robust spinel oxide OER catalysts.

Hydrogen has been proposed for long as an energy carrier for a sustainable and clean energy infrastructure. However, such a hydrogen energy infrastructure has not been realized yet even so many years have passed since its first proposal. One of the major reasons is the low efficiency and high material cost of water electrolysis, which is a mean to sustainably produce hydrogen fuel from water using the electrical energy generated by sustainable resources like solar panels.[1] The low energy efficiency of water electrolysis is mainly caused by the sluggish reaction kinetics at the anode,[2] where water is oxidized and the oxygen evolution reaction (OER) occurs. The benchmark anode electrocatalysts are noble metal-based oxides, such as IrO_2 and RuO_2,[3-4] which, however, aggravates the cost problem for water electrolysis. In recent years, great efforts have been made to explore first-row 3d transition metal oxides as low-cost alternatives for OER.[1, 5] One important progress is that the active sites are oxyhydroxides generated under operando condition.[6-10] Particularly, many Co-based oxides have been reported to undergo surface self-reconstruction of Co sites to Co (III) oxyhydroxides with the di-μ-oxo bridged Co-Co sites[11-12], offering a higher activity[6, 9]. However, how to properly facilitate the surface reconstruction is still elusive in literature. Furthermore, such surface reconstruction should be controlled in order to avoid to compromise all the bulk of the oxide catalyst, which serves as a template for the creation of the highly active surface. Thus, it is highly desired to develop strategies for activating and terminating the surface reconstruction.

Here, we report an approach to promote the surface reconstruction on inactive but low-cost $CoAl_2O_4$ (see Supplementary Note 1 for more about $CoAl_2O_4$) and to boost its OER performance by substituting Al with a small amount of Fe. The partially substituted $CoFe_{0.25}Al_{1.75}O_4$ outperforms IrO_2. We demonstrate here that a low level of Fe substitution is able to facilitate the surface

reconstruction of $CoAl_2O_4$ by activating the pre-oxidation of Co and optimizing the O 2p level of oxide for greater structural flexibility. More importantly, a distinctive reconstruction behavior with self-termination has been revealed on $CoFe_{0.25}Al_{1.75}O_4$, which enables a stable surface chemistry. In addition, we suggest that, on the reconstructed surface, the Fe substitution facilitates a two-step deprotonation process, which leads to the formation of active oxygen sites at a low overpotential and thus greatly promotes the OER. Finally, the electrolysis application of $CoFe_{0.25}Al_{1.75}O_4$ as OER catalyst was demonstrated in membrane electrode assembly (MEA) configuration.

Results

Crystal structure characterization

The $CoFe_xAl_{2-x}O_4$ (x=0~2.0) oxides were synthesized by a sol-gel method. The crystal structures of $CoFe_xAl_{2-x}O_4$ oxides were characterized by powder X-ray diffraction (XRD). As displayed in Fig. 1a, the diffraction peaks of the as-prepared $CoAl_2O_4$ and $CoFe_2O_4$ match well with that of the standard cubic spinel (Fd-3m) oxides. $CoFe_xAl_{2-x}O_4$ oxides with different Fe substitution amount remain in cubic spinel structure. Besides, the diffraction peak exhibits certain shift to lower angle with the increase of Fe substitution amount in the range of 0.25<x<2 (Supplementary Fig. 1). Such peak shift could be ascribed to changes in lattice parameters induced by different ionic radius of Fe and Al cations and suggests a solid solution property. However, when the Co local atomic structure was investigated by EXAFS (Fig. 1b, Supplementary Fig. 2), certain isobestic points, such as at 4.5 $Å^{-1}$, are remarkable, implying a complex property with Co in different components.[13] As further observed in Fourier transform (FT) Co K-edge EXAFS (Fig. 1c), two separated peaks, i.e. Peak II and Peak III, at 2.4~3.1 Å are assigned to the features of Co_{Oh} (in octahedral site) and Co_{Td}

(in tetrahedral site). At $x \leq 0.25$, no obvious changes are observed for peak II and peak III compared to pristine $CoAl_2O_4$, indicating that low-level Fe substitution does not change the occupation of Co. The obvious uplift of these two peaks starts from $x=0.5$, which could be attributed to the segregation of a component that comprises more octahedrally coordinated Co. This segregated component is inferred as $CoFe_2O_4$ which is in inversed spinel structure where Co occupy the octahedral site.[14] Such inference is further evidenced by a Co K-edge XANES linear combination fitting (LCF) with $CoAl_2O_4$, $CoFe_2O_4$ and $CoFe_{0.25}Al_{1.75}O_4$ as standard (Supplementary Fig. 3). The fitting delivers an extremely low R factor, indicating that Co is primarily in $CoAl_2O_4$, $CoFe_2O_4$ and $CoFe_{0.25}Al_{1.75}O_4$ components throughout the oxides.

In addition to the complex behavior of Fe-containing components throughout the oxides, the Fe substitution in $CoAl_2O_4$ also alters the local atomic structure of Co. As observed in Co K-edge EXAFS (Fig. 1c), the first-shell peak at ~1.5 Å, representative of the metal-oxygen bond, is weakened by Fe substitution, suggesting lower metal-oxygen coordination number and more oxygen vacancy[15]. Specifically, the EXAFS fitting result (Supplementary Table 1) of the first-shell peak for $CoFe_xAl_{2-x}O_4$ and $CoAl_2O_4$ reveals that Fe substitution reduced the average coordination number by ~0.4 at maximum. Such effect, indicating an increase in oxygen vacancy, is consistent with a decrease in cobalt valence state after Fe substitution which is evidenced by the shift to lower energy of the Co K-edge XANES (Fig. 1d). The nominal Co valence states (Supplementary Table 2) are indicated by the K-edge positions when compared to references $CoAl_2O_4$ and Co_3O_4 (see details in SI). While Fe^{3+} is more electronegative than Al^{3+}, after Fe substitution, the K-edge energies of Co slightly shift to lower absorption energy compared to $CoAl_2O_4$, indicating a decrease in Co valence state. This counterintuitive phenomenon could be rationalized by the creation of oxygen vacancies,[5] which is also supported by theoretical calculation (Supplementary Table 3). Indeed, the Fe substitution in $CoAl_2O_4$ was

found to reduce the formation enthalpy of oxygen vacancy, which indicates easier formation for oxygen vacancy.
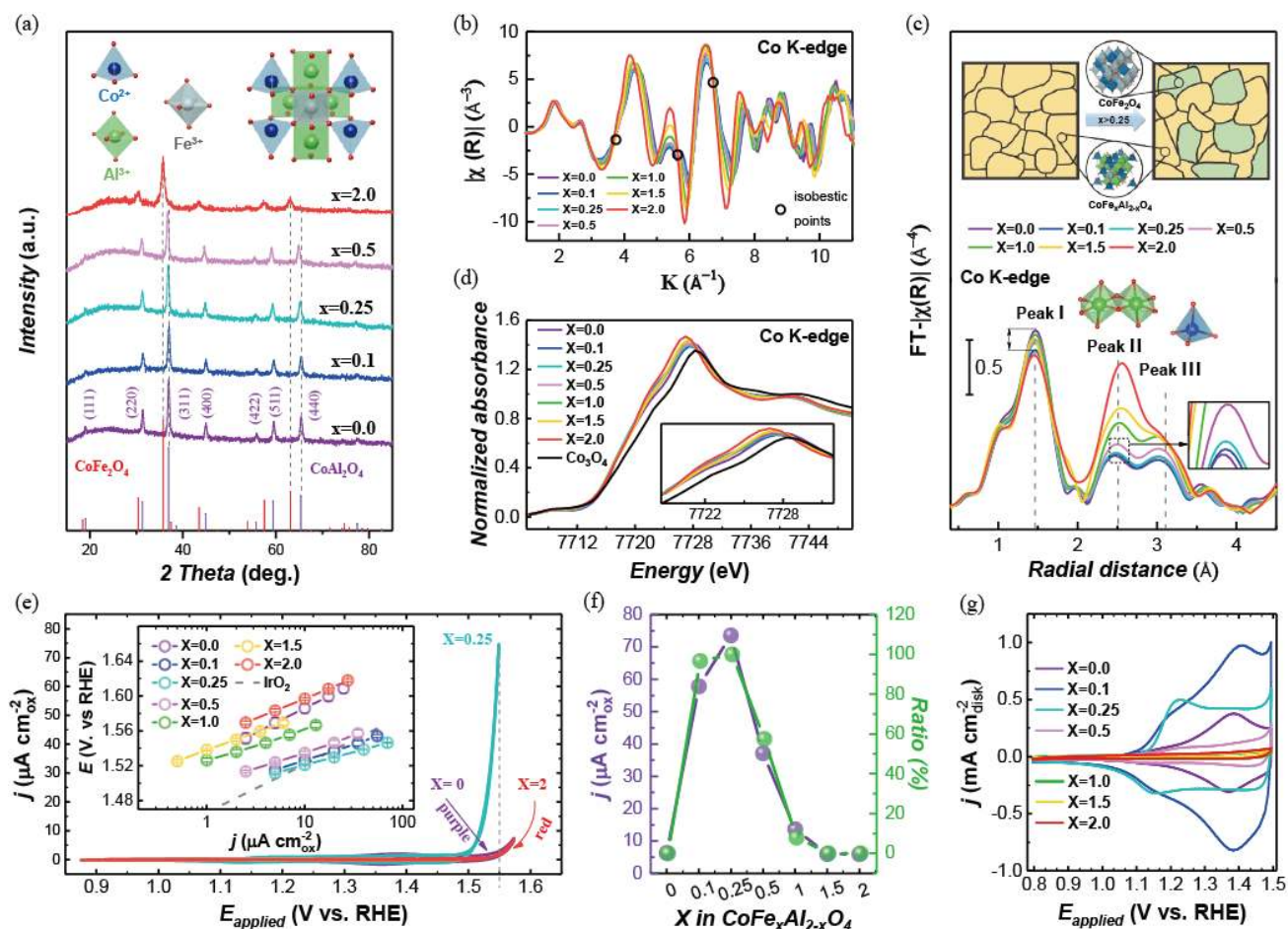

Fig. 1 | Structural characterizations and OER performances of as-prepared CoFe$_x$Al$_{2-x}$O$_4$ catalysts. a, The powder X-ray diffraction (XRD) patterns of as synthesized CoFe$_x$Al$_{2-x}$O$_4$ (x=0.0~2.0) oxides. **b,** The Co K-edge EXAFS spectra of CoFe$_x$Al$_{2-x}$O$_4$ (x=0.1~2.0). **c,** The Fourier transform (FT) k3χ(R) Co K-edge EXAFS of CoFe$_x$Al$_{2-x}$O$_4$ (x=0.1~2.0). The inset is schematics of the compositions in the CoFe$_x$Al$_{2-x}$O$_4$ oxide. **d,** The normalized Co K-edge XANES spectra of CoFe$_x$Al$_{2-x}$O$_4$ samples and the standard Co$_3$O$_4$ (Sigma Aldrich) as the references. The K-edge position is determined by an integral method[16] as described in Methods, and the details about edge positions and nominal valence state of Co and Fe are shown in Supplementary Table 2. **e,** The cyclic voltammetry curves of CoFe$_x$Al$_{2-x}$O$_4$ (x=0, 0.25, and 2) in O$_2$ saturated 1 M KOH with a scan rate of 10 mV s^{-1}. The inset is the corresponding Tafel plots after oxide surface area normalization, capacitance correction, and iR correction. The error bars represent the standard deviation from three independent measurements. The grey dashed line shows the best IrO$_2$ OER performance reported to date.[4] **f,** The OER current densities (left axis) of CoFe$_x$Al$_{2-x}$O$_4$ at 1.55 V vs. RHE. The composition ratio of CoFe$_{0.25}$Al$_{1.75}$O$_4$ component (right axis) in CoFe$_x$Al$_{2-x}$O$_4$ oxides is plotted to show its correlation with the OER activity. **g,** The cyclic voltammetry curves of CoFe$_x$Al$_{2-x}$O$_4$ (x = 0~ 2) in O$_2$ saturated 1 M KOH with a scan rate of 10 mV s^{-1} between 0.8 and 1.5 V vs RHE. The upper limit of the potential window is capped to show the pseudocapacitive behavior preceding to OER.

OER activity

The spinel $CoFe_xAl_{2-x}O_4$ oxides were then measured for their electrocatalytic OER performances under alkaline condition (see details in Methods). Supplementary Fig. 4 shows their steady OER cyclic voltammetry (CV) curves. The current density was normalized to the surface area of oxides to present the intrinsic activity, with the surface area of oxides being determined by Brunauer-Emmett-Teller (BET) measurements (Supplementary Fig. 5 and Supplementary Table 4). Ohmic drop iR correction was applied to compensate the potential loss from the resistance of the electrolyte solution. As observed in Supplementary Fig. 4, among these spinel oxides, $CoFe_{0.25}Al_{1.75}O_4$ is the best-performing one. Comparable OER performance is also observed for low-level Fe substituted oxides at x=0.1 and 0.5. In contrast, when further increasing the Fe substitution, significant drop in activity is found as x exceeds 0.5 in $CoFe_xAl_{2-x}O_4$. Fig. 1e shows the selected OER CV curves for x= 0, 0.25, and 2. Much better OER activity is found for x=0.25 than for x=0 and x=2. As seen in the Tafel plots given in the inset of Fig. 1e, the OER overpotential for $CoFe_{0.25}Al_{1.75}O_4$ (at 10 μA cm^{-2}_{oxide}) is approximately 70 mV lower than that for $CoAl_2O_4$ and $CoFe_2O_4$ (Supplementary Fig. 6). Such activity contrast indicates a special role of Fe in oxides at the low substitution level. In addition, IrO_2 previously benchmarked is also shown in the Tafel plot for comparison.[4] As observed, the electrocatalytic activity of the best-performing $CoFe_{0.25}Al_{1.75}O_4$ outperforms the activity of the benchmark IrO_2 catalyst. Long-term stability tests (Supplementary Fig. 7) of $CoFe_xAl_{2-x}O_4$ (x=0, 0.25 and 2) oxides were carried out at constant current density of 10 μA cm_{ox}^{-2} in 1 M KOH for 10 h. All measured samples exhibit negligible potential loss, which indicates a good stability for these spinel catalysts under OER conditions. The best-performing catalyst, $CoFe_{0.25}Al_{1.75}O_4$, was further carried Chronopotentiometry test for 48 hours under 20 μA cm_{ox}^{-2} (~3.5 mA cm_{disk}^{-2}). As shown in the Supplementary Fig. 8 a, b, the $CoFe_{0.25}Al_{1.75}O_4$ still shows negligible activity change after 48-hour test, which demonstrates a superior stability of $CoFe_{0.25}Al_{1.75}O_4$ in alkaline for OER.

Composition effect on OER

We then investigate the OER promotion at low substitution level and the detrimental effect at higher substitution level. Firstly, the $CoFe_{0.25}Al_{1.75}O_4$ component may primarily contribute to the OER activity according to the observed composition dependence. We then carried out LCF for the Co K-edge XANES using $CoFe_{0.25}Al_{1.75}O_4$ as standard in order to study the composition throughout the substituted oxides (Supplementary Fig. 3 and Supplementary Table 5). As found by the LCF (Fig. 1f, green line), the composition ratio of the $CoFe_{0.25}Al_{1.75}O_4$ component is abundant at low substitution level such as x=0.1 and 0.25 but become negligible as x $\geq$ 1. This trend correlates well with the OER activities of $CoFe_xAl_{2-x}O_4$ oxides (Fig. 1f, purple line). Thus, it suggests that the $CoFe_{0.25}Al_{1.75}O_4$ component is primarily responsible for the significant OER enhancement. Besides, the consistent trend is also observed for the pseudocapacitive charge in CV before OER region (Supplementary Fig. 9) which is quantified from CVs (Fig. 1g) by previously reported approaches.[17-18] The pseudocapacitive charge is particularly large at low substitution level but significantly decrease at high Fe substitution (x $\geq$ 1). The pseudocapacitive charge indicates the redox of surface active sites,[18] and its consistent trend with OER activities throughout the oxides suggests that the amount of active sites is a dominating factor for OER activity in our case. Thus, the strong correlation between OER activity and the composition ratio should be ascribed to the $CoFe_{0.25}Al_{1.75}O_4$ component, which may govern the formation of active sites.

Active site identification

Attention was then paid on the dynamic changes at metal sites during the electrochemical process. Note that there is nearly no change in the valency of Co and Fe in $CoFe_xAl_{2-x}O_4$ (Fig.1d, Supplementary Fig. 10, and Supplementary Table 2) and the local atomic structure of Fe site in $CoFe_{0.25}Al_{1.75}O_4$ remains unchanged under

OER (Supplementary Fig. 11). The pre-oxidation of Co (II) in $CoFe_{0.25}Al_{1.75}O_4$ during the potential sweeps is proposed to play a critical role in evolving active species (the preclusion of the pre-oxidation of Fe (III) to evolve active species is shown in SI). Earlier studies have revealed the importance of pre-oxidation of Co (II) in oxides for OER, where Co (II) is inclined to be oxidized to Co (III) or higher oxidation state, which is believed to be a critical step to generate active oxyhydroxide sites for OER.[19-20] To study the pre-oxidation of Co (II) in $CoAl_2O_4$ and $CoFe_{0.25}Al_{1.75}O_4$, their cyclic voltammetries (1st and 2nd cycles) are investigated (Fig. 2a). For both $CoAl_2O_4$ and $CoFe_{0.25}Al_{1.75}O_4$, the 1st cycle display a larger pseudocapacitive charge than 2nd cycle and the CV profiles exhibit negligible changes during subsequent cycles (Supplementary Fig. 12). Such electrochemical behaviors suggest that the surface of catalysts might undergo an irreversible surface reconstruction into, as reported, the oxyhydroxide[10], evolving a stable catalytic surface for OER. In addition, we found that the oxyhydroxide formation here displays different pseudocapacitive behaviors depending on the presence or not of Fe. To be specific, the anodic peak in 1st cycle appears at ~1.32 V for $CoFe_{0.25}Al_{1.75}O_4$, while a much more anodic one is observed for $CoAl_2O_4$ (~1.41 V), suggesting a promoting effect of Fe on the pre-oxidation of Co (II) and facilitating the subsequent formation of Co oxyhydroxide. For $CoFe_{0.25}Al_{1.75}O_4$, significant differences are observed between the 1st cycle and 2nd cycle in oxidation peak as well as the pseudocapacitive charge, indicating a change in surface chemistry, while no such marked contrast was observed for $CoAl_2O_4$. Thus, a more thorough reconstruction may happen on the surface of $CoFe_{0.25}Al_{1.75}O_4$. According to the aforementioned pseudocapacitive behaviors, such reconstruction should be ascribed to the presence of $CoFe_{0.25}Al_{1.75}O_4$ component. Then, as observed in the OER region, the overpotential for triggering the OER by $CoFe_{0.25}Al_{1.75}O_4$ is greatly reduced at 2nd cycle while almost no such difference is detected between 1st and 2nd cycle for $CoAl_2O_4$, indicating that the reconstruction process in the presence of Fe is a critical step for OER. In the 2nd and subsequent cycles, reversible redox peaks are observed for $CoAl_2O_4$ and

$CoFe_{0.25}Al_{1.75}O_4$ in pseudocapacitive range, suggesting reversible redox reactions on the reconstructed surfaces. For $CoAl_2O_4$, the major anodic peak appears at ~1.38 V, which could be assigned to Co (III) / Co (IV) transition as suggested in previous literature[21]. However, the Co (III) / Co (IV) transition cannot be rationalized without an earlier notable Co (II) / Co (III) anodic features (should appear at ~1.2 V vs RHE). Besides, its high intensity also contradicts the fact that only a small portion of Co cation in Co-based oxides could be reached and oxidized into Co (IV)[20, 22]. Considering that the surface has reconstructed during the 1st cycle, we believe that this anodic peak at ~1.38 V should be primarily attributed to the delayed Co (II) / Co (III) transition. Since the anodic process on oxyhydroxide surface can be viewed as deprotonation process with oxidation of metal cation,[12] the delayed Co (II) oxidation for $CoAl_2O_4$ suggests a difficult deprotonation process. For $CoFe_{0.25}Al_{1.75}O_4$, an obvious anodic wave is observed at ~ 1.2V which is assigned to Co (II) / Co (III) transition.[9, 21] This observation suggests an easier deprotonation process and activated Co (II) oxidation due to the Fe substitution. Such Co (II) / Co (III) redox is followed by a double layer charging response, which may result from the large surface area of the reconstructed surface and suggests a diffusion of a distribution of protons on the surface[23]. After such anodic redox of Co species, $CoFe_{0.25}Al_{1.75}O_4$ exhibit a much lower overpotential required for triggering OER than that for $CoAl_2O_4$ (~70 mV lower as indicated in Fig. 1e). Thus, it is clear that in the presence of Fe, highly active oxyhydroxides would be induced along with the reconstruction of oxide surface. Therefore, the Fe substitution is inferred to activate the Co pre-oxidation at low potential, facilitating both the surface reconstruction and the subsequent evolution of surface active sites. Such inference is further substantiated by *in-situ* XANES and the active species as identified by *in-situ* EXAFs.
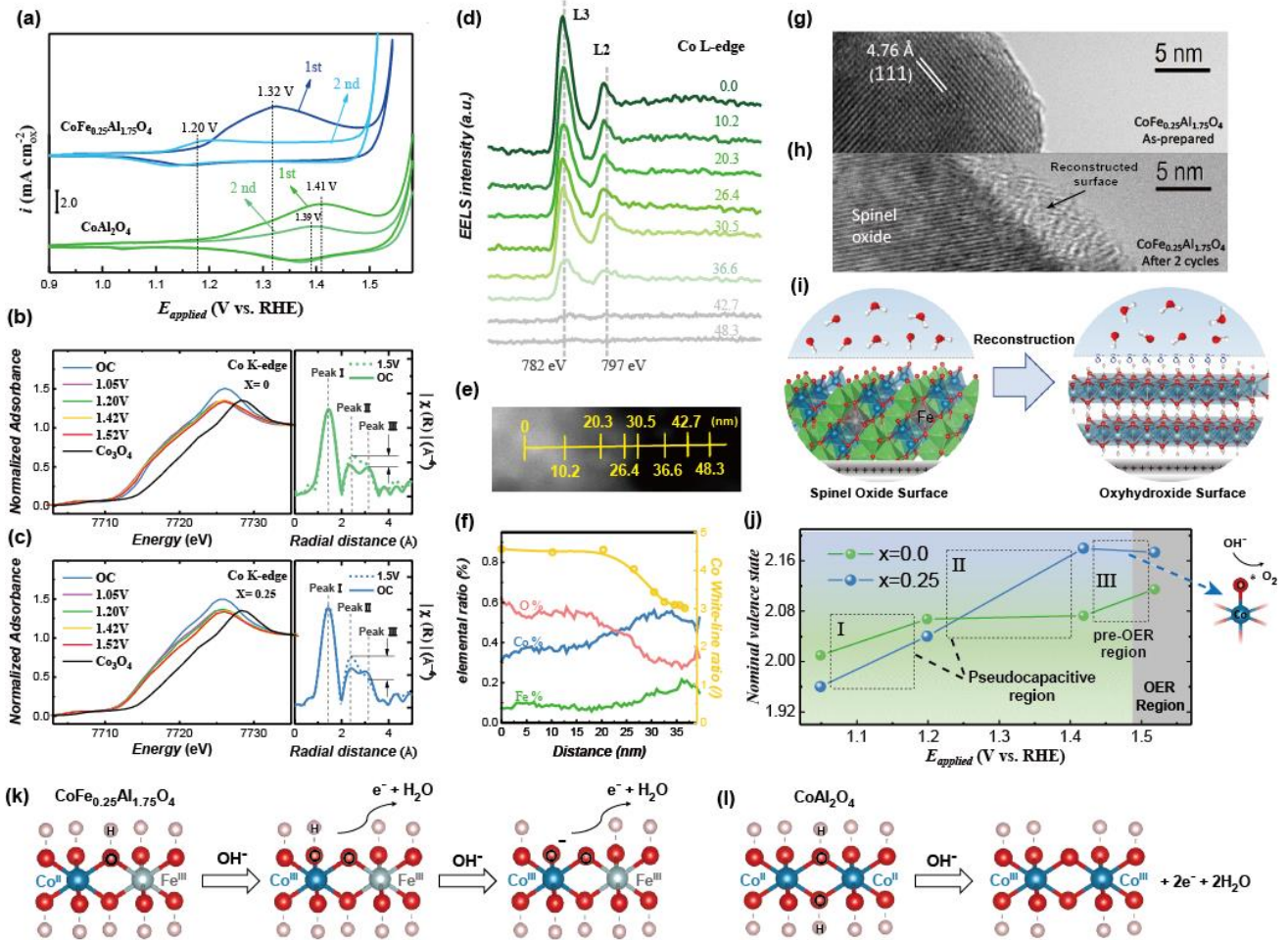
Fig. 2 | *in-situ* investigation on pre-OER behaviors of catalysts and schematic illustration of surface reconstruction and deprotonation process. a, The pseudocapacitive behavior in the 1st and 2nd cycles of $CoFe_{0.25}Al_{1.75}O_4$ and $CoAl_2O_4$ during the cyclic voltammetry cycling. **b,c,** The normalized in-situ Co K-edge XANES (left) under the different potentials of 1.05, 1.20, 1.42, and 1.52 V (vs. RHE) with Co_3O_4 (Sigma Aldrich) as the references, as well as the in-situ Fourier transform (FT) $k3\chi(R)$ Co K-edge EXAFs (right) under open circuit (OC) and 1.5 V (vs. RHE): **(b)** $CoAl_2O_4$ and **(c)** $CoFe_{0.25}Al_{1.75}O_4$. The peak I, II, and III in FT-EXAFS are assigned to M-O, M_{Oh}-M_{Oh}, and M_{Oh}-M_{Td} radial distance, respectively. **d,** The Co L-edge EELS spectra along with the line pathway as shown in **e,** scanning transmission electron microscopy (STEM) of $CoFe_{0.25}Al_{1.75}O_4$ after 100 cycles. The mark points denote the scanning distance along with the path way (nm): 0, 10.2, 20.3, 26.4, 30.1, 36.6, 42.7 and 48.3. **f,** The elemental ratio of O, Co, Fe (left axis) and the white-line ratio of Co L-edge (right axis) along with the line pathway. The white-line ratio is determined by the intensity of L3 and L2 peaks in EELS spectra.[24] **g,h,** The HRTEM images to show the surface regions for (g) as-prepared $CoFe_{0.25}Al_{1.75}O_4$; (h) $CoFe_{0.25}Al_{1.75}O_4$ after 2 cycles **i,** The reconstruction process from spinel $CoFe_{0.25}Al_{1.75}O_4$ into oxyhydroxide with activated negatively charged oxygen ligand. **j,** The *in-situ* Co oxidation state of $CoFe_{0.25}Al_{1.75}O_4$ and $CoAl_2O_4$ (i.e. x=0) under the different potentials of 1.05, 1.20, 1.42, and 1.52 V (vs. RHE). **k,l,** The proposed deprotonation mechanism before OER are shown for **(k)** $CoFe_{0.25}Al_{1.75}O_4$ and **(l)** $CoAl_2O_4$.

In Fig. 2b and 2c (right diagram), the *in-situ* Co K-edge Fourier transform (FT) EXAFS spectra without and

with an applied potential of 1.5 V (vs RHE) are shown for $CoFe_{0.25}Al_{1.75}O_4$ and $CoAl_2O_4$ (x=0). At open circuit, the FT-EXAFS profiles for $CoFe_{0.25}Al_{1.75}O_4$ and $CoAl_2O_4$ (x=0) are quite similar. The Peak I at ~1.5 Å is referred to an average metal-oxygen bond length. Two separated peaks, i.e. Peak II and Peak III at 2.4 Å and 3.1 Å, respectively, are assigned to the radial distance of Co_{Oh} (Co in octahedral site) and Co_{Td} (Co in tetrahedral site) to their neighboring metal atoms. Because the Co fraction does not change in $CoFe_xAl_{2-x}O_4$ with the Fe substitution, the ratio of Peak II to Peak III represents the composition ratio of Co_{Oh} and Co_{Td} in these oxides. Compared with the profiles collected at open circuit, the Peak II of Co K-edge in both $CoFe_{0.25}Al_{1.75}O_4$ and $CoAl_2O_4$ increase with the applied potential of 1.5 V. Such increase of the Peak II indicates an accumulation of Co atoms in edge-sharing octahedral coordination[8], which is attributed to the formation of Co oxyhydroxide which is in edge-sharing CoO_6 octahedral structure.[20] Notably, a much higher ratio of Peak II / Peak III is observed for $CoFe_{0.25}Al_{1.75}O_4$ as compared to that for $CoAl_2O_4$, suggesting a consistent conclusion as our observation in 1st cycle of CV that the reconstruction into oxyhydroxide is more thorough for $CoFe_{0.25}Al_{1.75}O_4$. Such reconstruction of Co on the surface for $CoFe_{0.25}Al_{1.75}O_4$ is also evidenced by STEM-EELS (Fig. 2d and 2e) and HRTEM (Fig. 2g and 2h) at the reconstructed surface. Under STEM-EELS, a notable increase of elemental ratio of Co (Co%) at the near surface of $CoFe_{0.25}Al_{1.75}O_4$ particles is detected (Supplementary Fig. 13 and Fig. 2f), which would be a result of Co oxyhydroxide formation on surface. The white-line ratio for Co L edge (Fig. 2f) decreases and indicates increased oxidation state[25], which could be an effect of irreversible of electrochemical oxidation of Co (II) to form Co (III) oxyhydroxide during the 1st cycle. Under HRTEM, the generated oxyhydroxide can be observed on the reconstructed surface of oxide. Thus, the surface chemistry of $CoFe_{0.25}Al_{1.75}O_4$ is changed by reconstruction from oxide into oxyhydroxide (Fig. 2i). As reported that Co oxyhydroxides evolved as the active species for many Co-based oxide catalysts,[7, 9-10, 19] we thus believe that the reconstruction facilitated by Fe substitution is

the most critical step for evolving active surface oxyhydroxide.

In the cases of active oxyhydroxides, some studies proposed a so-called active oxygen species,[26-28] which is created during the deprotonation (anodic sweep) step, as the ultimate active site. Thus, considering the observed alternation of anodic peak by Fe substitution in 2nd CV cycle, the dynamic valence state of Co during the anodic sweep was then examined by *in-situ* XANES. Fig. 2b and 2c (left diagram) display the Co K-edge XANES of $CoFe_{0.25}Al_{1.75}O_4$ and $CoAl_2O_4$ (x=0) oxides recorded at 1.05, 1.20, 1.42, and 1.52 V (vs. RHE), respectively. The K-edges in XANES of both oxides shift to higher energy, indicating the oxidation of Co. The corresponding nominal valence states of Co in $CoFe_{0.25}Al_{1.75}O_4$ and $CoAl_2O_4$ under each applied potential are plotted in Fig. 2j. The valency increment in the pseudocapacitive region could be primarily observed in region I (1.05 – 1.20 V) and region II (1.20 – 1.42 V), and the Co behavior in pre-OER stage can be found in region III (1.42 – 1.52 V). The increase of Co valency could be viewed as deprotonation process on the reconstructed surface of catalysts. As observed, in pseudocapacitive range (region I and region II), the $CoFe_{0.25}Al_{1.75}O_4$ exhibits an increase of valency in both region I and region II. Whereas, the valency for $CoAl_2O_4$ increases only in region I, suggesting a limited deprotonation process. Its next deprotonation process is only observed at higher potential in the region III. Thus, the Fe substitution is likely to facilitate the deprotonation process at low potential to form active oxygen species on the surface, which accounts for the OER activity enhancement. Here, to illustrate the role of Fe in deprotonation process, we propose two proton/electron transfer processes for evolving active oxygen sites on $CoFe_{0.25}Al_{1.75}O_4$ surface. As shown in the Fig. 2k, the first deprotonation process on $CoFe_{0.25}Al_{1.75}O_4$ should start at the bridged OH linked to both Co and Fe center, which is responsible for the valency increment of Co (II) cation, and such process on bridged OH could be facilitated

by its neighboring Fe^{3+} center. The first deprotonation process is followed by another deprotonation process at terminal OH linked to Co or Fe center. Similar deprotonation process was also reported for $NiFe_xOOH$[27]. Unlike $NiFe_xOOH$ where the Fe substitution anodically shifts the Ni oxidation peak[12, 27], an opposite behavior was observed here for Fe substituted $CoAl_2O_4$. The suppressing effect of Fe on Ni oxidation was explained by the kinetics barrier for the deprotonation of terminal OH linked to Fe center.[12] Thus, on the basis of the activated Co oxidation in our study, we believe that the second deprotonation process should be at the terminal OH linked to Co center, and the activated Co oxidation is ascribed to the reduced kinetic barrier for the proton abstraction at Co site. The second process with one proton abstraction is not compensated by the metal oxidation but rather by negatively charged oxygen ligand (O*) that serves as active site. However, for $CoAl_2O_4$, during the corresponding pseudocapacitive range, it merely undergoes deprotonation process on bridged OH (Fig. 2l). The following deprotonation for $CoAl_2O_4$ on the terminal OH is greatly delayed and OER does not occur till the second deprotonation happens, suggesting this process as a prerequisite for OER. Thus, the critical role of Fe is to facilitates the deprotonation process to generate active oxygen site at lower potential on $CoFe_{0.25}Al_{1.75}O_4$, thereby leading to a lower overpotential for OER. It should be noted that the redox reaction on the reconstructed oxyhydroxide surface would be greatly affected by the reconstruction process in the 1st cycle. As also observed in our pH dependence measurement (Fig. 3a), the redox peak is greatly altered, not simply shifted, by changing the pH of electrolyte. Especially, the redox peak is even muted at pH ≤ 13. Clearly, such alternation is led by a pH-sensitive surface reconstruction, which results in forming surface oxyhydroxide in different state with varied pH. Such pH-sensitive surface reconstruction suggests that it may include certain decoupled proton/electron transfer process such as lattice oxygen oxidation[29] which is further demonstrated in the following section.
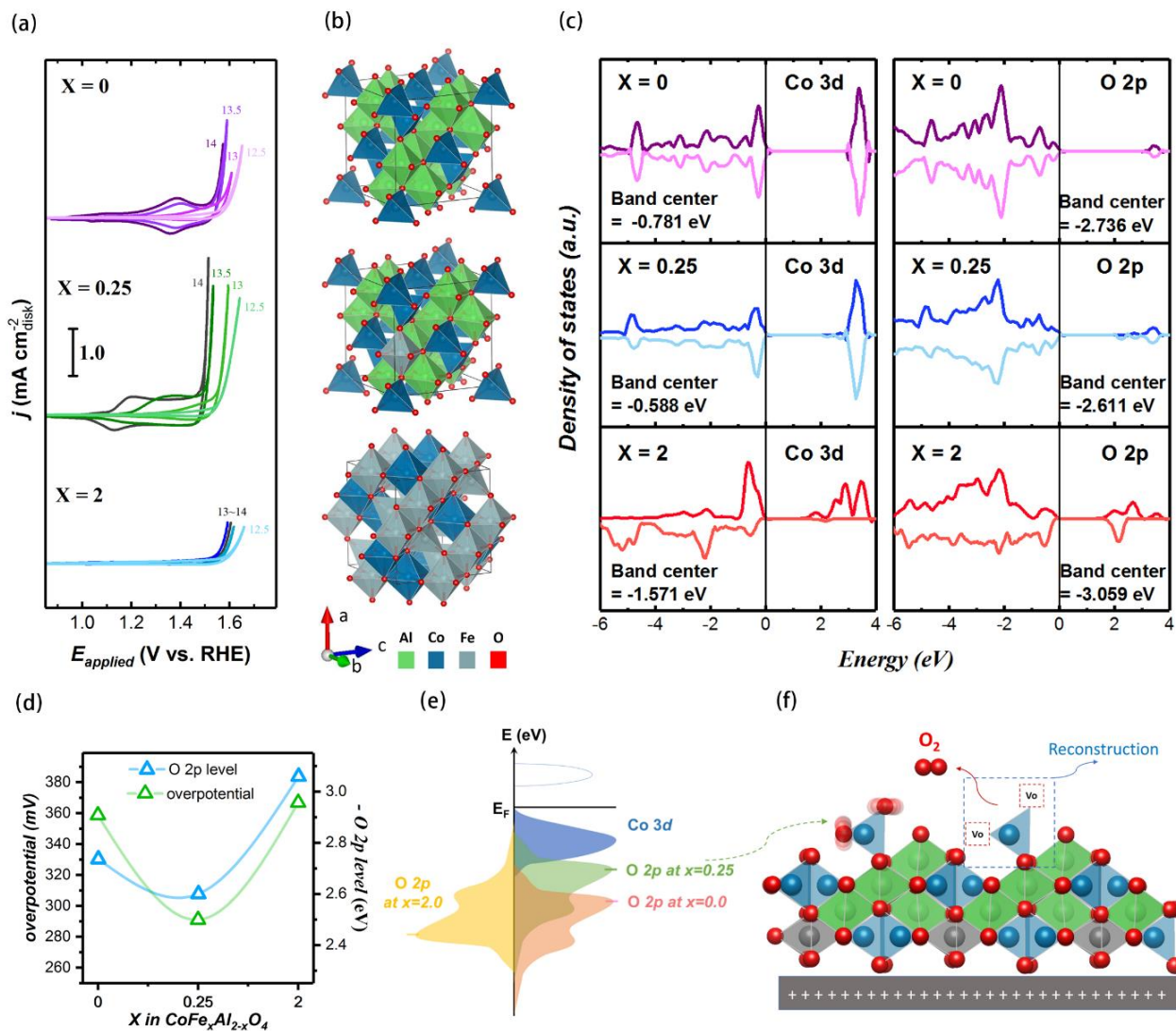
Fig. 3 | Electronic interpretation of the effect of Fe substitution on surface reconstruction. a, Cyclic Voltammetry (CV) of $CoFe_xAl_{2-x}O_4$ (x=0.0, 0.25 and 2.0) scanned in O_2-saturated KOH (pH= 12.5~14) at a scan rate of 10 mV s^{-1}. **b,** The computational models of $CoFe_xAl_{2-x}O_4$: (top) x=0, (middle) x=0.25, (Bottom) x=2. **c,** The computed Co 3d, O 2p density of state (PDOS) of $CoFe_xAl_{2-x}O_4$ (x=0, 0.25 and 2.0). **d,** The OER overpotential at 10 μA cm$^{-2}_{oxide}$ and the O 2p band center relative to Fermi level (-O 2p) for $CoFe_xAl_{2-x}O_4$ (x=0.0, 0.25 and 2.0) **e,** The schematic band diagrams of $CoFe_xAl_{2-x}O_4$ (x=0, 0.25 and 2.0). The Co 3d-band in the diagram represents the highest occupied state and the lowest unoccupied state. **f,** The schematic diagram of a surface reconstruction mechanism for $CoFe_{0.25}Al_{1.75}O_4$.

Interpretation of O 2p

As aforementioned, the active oxygen site is generated by the deprotonation on the oxyhydroxide surface and

the reconstruction for forming surface oxyhydroxide serves as the prerequisite for efficient OER catalysis. We

have also mentioned that the Fe-facilitating reconstruction is dominated by the $CoFe_{0.25}Al_{1.75}O_4$ component and may involve certain decoupled proton/electron transfer process. The inner driving force for the reconstruction is further studied by density functional theory (DFT) calculation. The electronic density of state (DOS) calculation is adopted to examine the alternation in electronic structure of oxides by Fe substitution. The computational models for $CoFe_xAl_{2-x}O_4$ (x=0, 0.25, and 2) are shown in Fig. 3b (see modelling and calculation details in SI). The projected density of state (pDOS) of $CoFe_xAl_{2-x}O_4$ (x=0, 0.25, and 2) oxides and their band center energies are given in Fig. 3c (see more details in Supplementary Table 6). As found for band center energies, the Fe substitution in $CoAl_2O_4$ uplifts the O 2p-band center in energy closer to the Fermi level. However, as Al^{3+} is fully replaced by Fe^{3+} to form $CoFe_2O_4$, it becomes an inverse spinel structure and the O 2p-band center greatly moves down in energy. The PDOS results reveal that Fe substitution could either uplift or downshift the O 2p level depending on the substitution level. Moreover, the position of O 2p-band center relative to Fermi level shows consistent trend with the OER activity of $CoFe_xAl_{2-x}O_4$ oxides (x=0, 0.25 and 2) (Fig. 3d). It is also noteworthy that the OER activity of $CoFe_xAl_{2-x}O_4$ oxides is greatly affected by their reconstruction process under OER conditions. Thus, the O 2p level is likely an influential factor to the surface reconstruction. Earlier studies have revealed that the O 2p-band level relative to the Fermi level was always associated with some activity-related structural parameters for perovskite oxides.[30-33] For example, a linear relationship was established between the O 2p-band level and the oxygen vacancy ($V_O^{\bullet\bullet}$) formation energy in some perovskite oxides, in which the low $V_O^{\bullet\bullet}$ formation energy could be predicted by high O 2p level close to Fermi level.[30-31] Given that spinel structure contains octahedral MO_6 unit as well as that of perovskite oxides,[5,34] the uplifted O-2p band center by Fe substitution should also facilitate the $V_O^{\bullet\bullet}$ formation in spinel oxides. Consistent results have been revealed above in the structural analysis of substituted oxides where Fe substitution lowers the metal-oxygen coordination number and decrease the Co valence state, suggesting an

increased oxygen vacancy concentration. In addition to the influential role of O 2p level on bulk $V_O^{\bullet\bullet}$ formation, it is also governing the lattice oxygen oxidation mechanism for oxides.[29, 35-36] With the uplifted O 2p center closer to Fermi level, the oxygen character in the antibonding state below Fermi level becomes more dominant (Fig. 3e). As an anodic potential is applied, the Fermi level shifts deeper into O 2p state and the holes in oxygen state are created as the O_2/H_2O redox potential is aligned with the O 2p state energy in the oxide, which leads to the oxidation of lattice oxygen.[29, 37] Thus, credited to the uplifted O 2p level, the oxidation of lattice oxygen in $CoFe_{0.25}Al_{1.75}O_4$ should be more favorable than that in $CoAl_2O_4$ and $CoFe_2O_4$. Note that the lattice oxygen mediated OER mechanism should not dominate the OER here. This is also confirmed by a cycling test of $CoFe_{0.25}Al_{1.75}O_4$ oxides over 100 cycles (shown in Supplementary Fig. 12). The lattice oxygen-mediated OER is always featured with unstable oxide due to cation leaching on catalysts and thus leading to activity increase with cycling.[36] For example, $Ba_{0.5}Sr_{0.5}Co_{0.8}Fe_{0.2}O_{3-\delta}$ (BSCF) as well-identified oxygen active-perovskite catalysts exhibit ~4-fold current increase over 50 cycles.[38] In contrast, the $CoFe_{0.25}Al_{1.75}O_4$ did not exhibit marked OER current variation during CV cycling, suggesting that the reconstructed surface is stable and the involvement of lattice oxygen is not notable during the OER catalysis. This is further evidenced by the electrochemical study on active surface area and HRTEM (Fig. 2g, 2h and Supplementary Fig. 14) of $CoFe_{0.25}Al_{1.75}O_4$ after reconstruction and 100 cycles. The reconstruction in 1st cycle is found merely at limited depth (~5 nm) on the surface of $CoFe_{0.25}Al_{1.75}O_4$ and the reconstructed surface keeps quite stable during subsequent cycling. Please also see detailed discussion in Supplementary Note 2. Thus, the stable surface chemistry after reconstruction excludes the involvement of lattice oxygen in OER catalysis on the reconstructed surface, and also keeps the accuracy of the estimation of the specific activity normalized to BET surface area. However, we believe that the surface reconstruction should start with the lattice oxygen oxidation, which results in the aforementioned pH-sensitive reconstruction (Fig. 3a). According

to early report, high $V_O^{\cdot\cdot}$ (oxygen vacancies) concentration (especially $V_O^{\cdot\cdot}$ on the surface) would grant structural flexibility for surface reconstruction on oxides.[6] As a further step, even though the induced $V_O^{\cdot\cdot}$ grants certain structural flexibility in oxides, these $V_O^{\cdot\cdot}$ are actually stabilized in the bulk crystal. In another word, such flexibility has to be triggered by additional perturbation such as the lattice oxygen oxidation. This is also evidenced by our theoretical study and XANES result of $CoFe_2O_4$, where $CoFe_2O_4$ exhibits the lowest enthalpy for oxygen vacancy formation (Supplementary Table 3) and experimentally possessing the highest oxygen vacancy concentration (Supplementary Table 2) compared to $CoAl_2O_4$ and $CoFe_{0.25}Al_{1.75}O_4$. However, neither an obvious reconstruction-related current response in the first cycle nor a redox peak subjected to oxyhydroxide during the second cycle can be observed for $CoFe_2O_4$ in CV (Supplementary Fig. 15). Besides, compared to $CoAl_2O_4$ and $CoFe_{0.25}Al_{1.75}O_4$, $CoFe_2O_4$ shows the weakest pH-dependent OER performance (Fig. 3a) and the lowest O 2p band center. Thus, we believe that the lattice oxygen oxidation at the pristine surface to creating more surface $V_O^{\cdot\cdot}$ should be a critical trigger for the surface reconstruction. This is further evidenced by the elemental ratio on the surface of $CoFe_{0.25}Al_{1.75}O_4$ after 100 cycles obtained by STEM-EELS (Fig. 2f). The O% greatly decreases along with notable Co enrichment on the reconstructed surface, which implies the critical role of creating surface oxygen vacancy on triggering Co reconstruction. Thus, it is believed that, along with the lattice oxygen oxidation,[29] a great structural instability emerges as the oxygen vacancies further accumulate on the oxide surface and induce the surface reconstruction (Fig. 3f) into oxyhydroxides that is more stable in alkaline.[39-40] As a result, such dynamic instability in electrochemical process can be electronically indicated by the O 2p level.
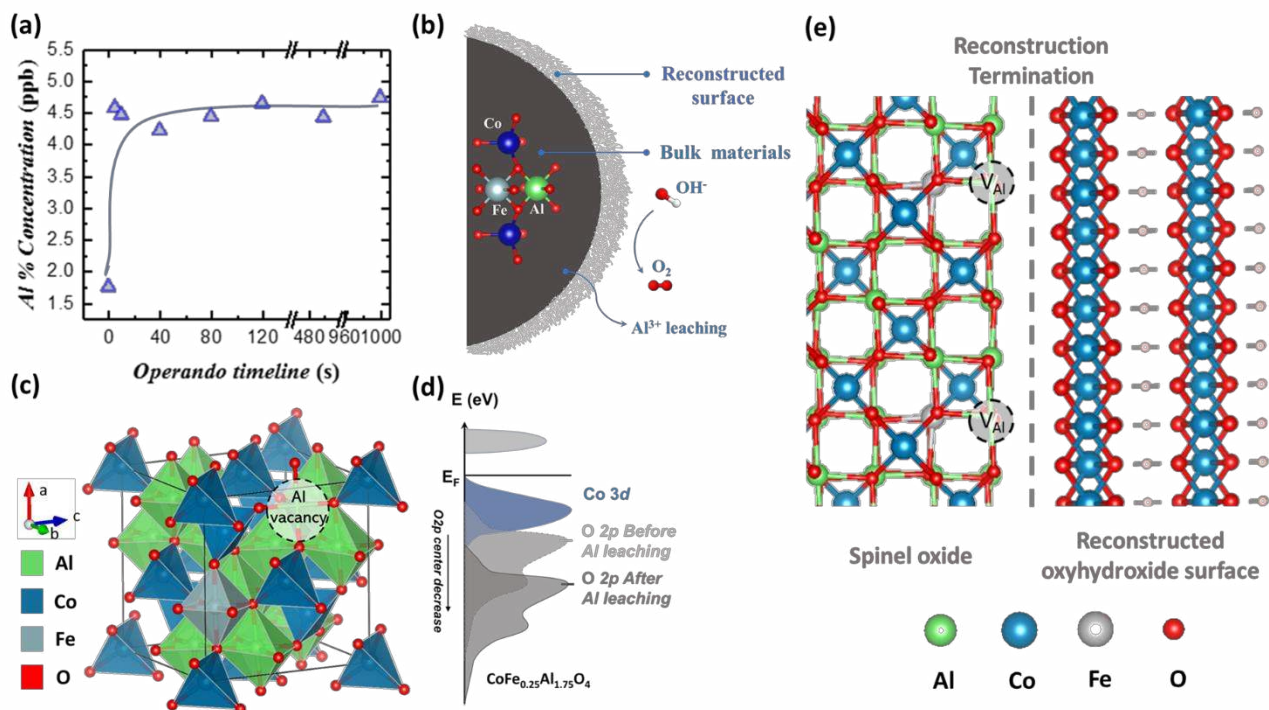
Fig. 4 | Reconstruction terminating mechanism with Al^{3+} leaching. a, ICP-MS test of the electrolyte for $CoFe_{0.25}Al_{1.75}O_4$ cycling under operation time of 0~1000s (in 1 M KOH under 20 μA cm_{ox}^{-2}). The dissolubility of Al in terms of $Al(OH)_4^-$ is far beyond the concentration of Al^{3+} in our tested electrolytes. **b,** The schematic of Al^{3+} leaching along with surface reconstruction of spinel oxide. **c,** The computational model for $CoFe_{0.25}Al_{1.75}O_4$ after Al^{3+} leaching. The spinel structure beneath reconstructed surface was confirmed under HRTEM (Supplementary Fig. 14b). **d,** The schematic band diagrams of $CoFe_{0.25}Al_{1.75}O_4$ with and without Al^{3+} vacancy. **e,** The schematic of $CoFe_{0.25}Al_{1.75}O_4$ that terminates its surface reconstruction due to the termination of lattice oxygen oxidation.

Also importantly, while many reconstructable catalysts like $Ba_{0.5}Sr_{0.5}Co_{0.8}Fe_{0.2}O_{3-\delta}$ exhibit unstable surface chemistry and become notably amorphous after cycling[38], $CoFe_{0.25}Al_{1.75}O_4$ is distinguished for its stable surface chemistry after reconstruction as discussed above. The reconstruction triggered by lattice oxygen oxidation was terminated after 1st cycle and the reconstructed surface is highly active and stable in the subsequent cycles. To investigate the mechanism of such reconstruction termination, we carried ICP test on the electrolyte used for $CoFe_{0.25}Al_{1.75}O_4$ cycling. It was found that the leaching of Al cations was notable while Co and Fe cations both exhibited negligible leaching (Supplementary Table 7). Besides, observed under operando timeline, the Al leaching was found quickly finished as the OER happened, and no notable Al

leaching is found thereafter (Fig. 4a), which is consistent with the reconstruction process observed in CV. Hence, we believe that the leaching of Al is closely associated with the reconstruction process. As Al leached with the reconstruction at the very beginning, such leaching would alter the local electronic structures of oxide to prevent further reconstruction (Fig. 4b). We further employed DFT to study the local electronic structure for the lattice with Al vacancy (Fig. 4c). As illustrated in Fig. 4d and Supplementary Fig. 16, the O 2p level decreases in energy as Al vacancy is introduced in the lattice. As a result, the lattice oxygen oxidation would be terminated as O 2p level is low in energy, and the reconstruction thus stops accordingly as no more oxygen vacancies created (Fig. 4e). Such termination mechanism makes $CoFe_{0.25}Al_{1.75}O_4$ a discernable catalyst which shows a stable surface chemistry after reconstruction and is capable to carry efficient and stable OER catalysis on reconstructed surface.
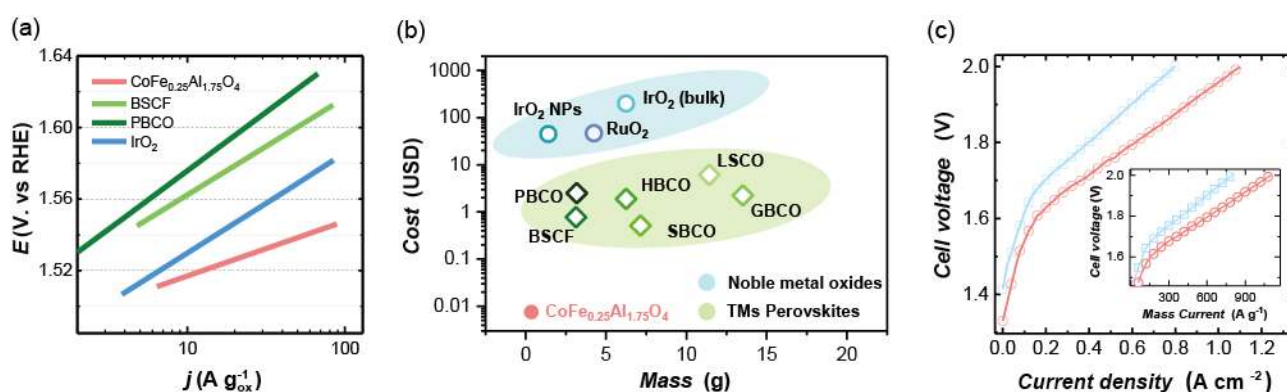

Fig. 5 | Competitive potential in electrolyzers application. a, Mass activity of $CoFe_{0.25}Al_{1.75}O_4$, $Ba_{0.5}Sr_{0.5}Co_{0.8}Fe_{0.2}O_{3-\delta}$ (BSCF)[1], $Pr_{0.5}Ba_{0.5}CoO_{3-\delta}$ (PBCO)[33] and IrO_2 nanoparticles (NPs)[4]. **b,** The material mass and cost for delivering a current of 10 A at overpotential of 0.3 V by $CoFe_{0.25}Al_{1.75}O_4$, $Ba_{0.5}Sr_{0.5}Co_{0.8}Fe_{0.2}O_3$ (BSCF)[1], $(Pr_{0.5}Ba_{0.5})CoO_{3-\delta}$ (PBCO)[33], $(Sm_{0.5}Ba_{0.5})CoO_{3-\delta}$ (SBCO)[33], $(Gd_{0.5}Ba_{0.5})CoO_{3-\delta}$ (GBCO)[33], $(Ho_{0.5}Ba_{0.5})CoO_{3-\delta}$ (HBCO)[33], IrO2 nanoparticles (NPs)[4], IrO_2 (bulk, Premetek Co.)[41] and RuO_2[42]. The cost is evaluated by the cost of metal elements in oxides. **c,** The polarization curves of the electrolyzer with $CoFe_{0.25}Al_{1.75}O_4$ (1 mg cm^{-2}) and IrO_2 (Premetek Co., 1 mg cm^{-2}) as anode catalyst and Pt/C (TKK 47.1 wt% Pt, 1 mg cm^{-2}) as cathode catalyst. Inset is the polarization curves of $CoFe_{0.25}Al_{1.75}O_4$ and IrO_2 in mass current density. Cell temperature was maintained at 60 $^\circ$C. The experimental details are shown in Methods.

With all advantages discussed above, $CoFe_{0.25}Al_{1.75}O_4$ exhibits competitive potential in alkaline electrolyzer applications. Its mass activity (Fig. 5a) outperforms IrO_2 and the benchmarked transitional metal oxides (e.g. $Ba_{0.5}Sr_{0.5}Co_{0.8}Fe_{0.2}O_{3-\delta}$ [1] and $Pr_{0.5}Ba_{0.5}CoO_{3-\delta}$[33]). Its cost for given performance is lower than that of noble

metal oxides and other reported transition metal perovskites by orders of magnitude (Fig 5b). $CoFe_{0.25}Al_{1.75}O_4$ was further examined in a homemade membrane electrode assembly (MEA) electrolysis cell with an anion exchange membrane as the solid electrolyte (Supplementary Fig. 17). The $CoFe_{0.25}Al_{1.75}O_4$ exhibited a notable higher mass efficiency as well as higher areal activity than IrO_2 (Fig. 5c). Its performance in MEA is also better than that reported for $Ba_{0.5}Sr_{0.5}Co_{0.8}Fe_{0.2}O_{3-\delta}$ under similar condition (Supplementary Fig. 18).[6]

Conclusion

In summary, we show a promoted surface reconstruction on $CoAl_2O_4$ by Fe substitution. $CoFe_{0.25}Al_{1.75}O_4$ is proven to be a critical component in the $CoFe_xAl_{2-x}O_4$ (x=0.0~2.0) series as it undergoes surface reconstruction. The surface reconstruction has been investigated by HRTEM, EELS, and XAFS. Evidenced by operando XAFS, Fe activates two deprotonation processes in reconstructed oxyhydroxides, leading to the formation of active oxygen species at a low overpotential. We interpret that the uplift of O 2p level by Fe substitution facilitates the creation of surface oxygen vacancies ($V_O^{\bullet\bullet}$) along with the lattice oxygen oxidation under OER condition and grants a greater structural flexibility for reconstruction. The O 2p moves down as Al^{3+} leaches at the beginning of reconstruction and further terminates the surface reconstruction for a stable surface chemistry. Under this strategy, $CoFe_{0.25}Al_{1.75}O_4$ exhibits outstanding intrinsic activity, mass efficiency, and stability toward OER. Its high performance has been also demonstrated in MEA configuration. On the basis of this work, more alternative strategies would be explored to tune the active sites formation by adjusting its dynamic reconstruction to develop robust and low-cost OER catalysts.

Methods

Materials synthesis and characterization. $CoFe_xAl_{2-x}O_4$ (x=0, 0.1, 0.25, 0.5, 1, 1.5, 2) powders were prepared by the sol-gel method using citric acid as a chelating agent and urea as combustion agent. Firstly, cobalt acetate ($Co(OAc)_2 \cdot 4H_2O$), Iron(III) nitrate nonahydrate ($Fe(NO_3)_3 \cdot 9H_2O$), aluminum nitrate ($Al(NO_3)_3 \cdot 9H_2O$) in specific molar ratio were dissolved in diluted nitric acid, followed by the addition of citric acid and urea. The mixture was stirred and heated up at 80-100 ºC to generate highly viscous gel. Then, the gel was then transferred to an oven to decompose and dry in the air at 170 ºC for 12 hours. Finally, followed by the calcination at 400 °C for 6 hours, the spinel $CoFe_xAl_{2-x}O_4$ (x=0, 0.1, 0.25, 0.5, 1, 1.5, 2) oxides were obtained. The High resolution TEM (HRTEM) and STEM-EELS were taken on a JEOL JEM- 2100F microscope at 200KV. The X-ray diffraction (XRD) patterns of

bulk $CoFe_xAl_{2-x}O_4$ were recorded on Bruker D8 diffractometer at a scanning rate of 2° min⁻¹, using Cu-Kα radiation (λ = 1.5418 Å). The BET (Brunauer-Emitter-Teller) surface area was analyzed on ASAP Tristar II 3020 from single-point BET analysis performed after 12 h outgassing at 170 °C (**Supplementary Table 4**).

Electrochemical characterization under three-electrode system. The working electrode was fabricated by drop casting method. The as-prepared catalysts which first mixed with acetylene black (AB) at a mass ration of 5:1, then were dispersed in isopropanol/water (v/v=1:4) solvent followed by the addition of Na^+-exchanged Nafion as the binder and ultrasonicated for 20min to form homogeneous ink. The glassy carbon electrode was polished to a mirror finish with 50 nm α-Al_2O_3 and ultrasonicated in IPA and water to completely clean up. At last, 10 μl of the as-prepared ink was dropped onto a glassy carbon (GC) electrode (0.196 cm²) and dried overnight at room temperature to yield a final loading mass of 255 μg_{ox} cm⁻².

The electrochemical tests were carried out by three-electrode method using $CoFe_xAl_{2-x}O_4$ as working electrode, platinum plate (1×2 cm²) as the counter electrode, Hg/HgO (1M KOH, aqueous, MMO) as the reference in O2-saturated 1.0 M KOH by using Bio-logic SP 150 potentiostat. All potentials are converted to RHE scale and iR corrected by the resistance of electrolyte. The conversion between the potentials vs. RHE and vs. MMO was performed by the following equation: E (vs. RHE) = E (vs. MMO) + E_{MMO} (vs. SHE) + 0.059 × pH. E_{MMO} (vs. SHE) = 0.098 vs. SHE at 25°C. The Cyclic Voltammetry(CV) was obtained under potentials from 0.875V to 1.575V (vs. RHE) at a scan rate of 10mV s⁻¹. Besides, the CV was also conducted for all samples under potentials from 0.695V to 1.495V (vs. RHE) to investigate the pseudocapacitive charge preceding the OER region. The chronopotentiometry measurement was performed by holding the specific current density of 10 μA cm⁻²$_{oxide}$ for 10 hours. Electrochemical impedance spectra(EIS) was recorded at 1.525V (vs. RHE) under 10 mV of amplitude from 100 KHz to 0.01Hz.

X-ray absorption spectroscopy. X-ray absorption near edge spectroscopy (XANES) and extended X-ray absorption fine structure (EXAFs) were performed under transmission mode at Singapore Synchrotron Light Source, XAFCA beamline. The Co and Fe K-edge position obtained by an integrate method [16] is shown in Supplementary Table 2. The Co nominal valence state is obtained by using as-prepared $CoAl_2O_4$ (+2.0, 7717.41 eV) and standard Co_3O_4 (+2.67, 7719.96 eV) as benchmark. The Fe nominal valence is obtained by using standard Fe_3O_4 (+2.67, 7121.71 eV) and standard Fe_2O_3 (+3, 7122.82 eV) as benchmark. Noted that the as-prepared $CoAl_2O_4$ well match with the standard $CoAl_2O_4$, and Co valence state in standard $CoAl_2O_4$ is +2. The nominal oxygen vacancy concentration is calculated on the basis of the nominal valence state of Co, Al (III) and Fe. The in-situ XAS measurements were performed in fluorescence-transmission geometry, where the spectra of samples and references were measured in fluorescence mode. The catalysts were sprayed on carbon paper at a loading of 2mg cm⁻² as working electrode. The measurement was carried out under the same condition as OER measurement in a homemade cell. The *in-situ* XANES measurement was applied after one cycle. The *in-situ* XAFS measurement was taken on the as-prepared catalysts without any additional electrochemical treatment. Acquired XAFS data were processed in ATHENA program and analysed in ARTEMIS program integrated with IFEFFIT software package[43].

Density functional theory calculations. The calculation was carried out by Vienna ab initio Simulation package (VASP) using spin-polarized density functional with the Hubbard model (DFT+U).[44-45] The projector augmented wave (PAW) model with Perdew-Burke-Ernzerhof (PBE) function was used to describe the interactions between core and electrons, and the value of the correlation energy (U) was fixed at 3.3, 4.3 eV for the 3d orbits of Co and Fe, respectively.[46-47] An energy cutoff of 500 eV was used for the plane-wave expansion of the electronic wave function. The Brillouin zones of all systems were sampled with Gamma-point centered Monkhorst-Pack grids. A 7×7×7 Monkhorst Pack k-point setup were used for bulk geometry optimization, while 9×9×9 for electronic structures calculation. The force and energy convergence criterion were set to 0.02 eV Å⁻¹ and 10⁻⁵ eV, respectively. All models are created by comparing the stability of spinel with normal or inversed structure in a unit cell, and the structures at lower energy are selected for study. The $CoAl_2O_4$ (Supplementary Table 7) prefer the normal spinel structure with Co^{2+} located on tetrahedral sites and the Al^{3+} located on octahedral sites ($[Co]_{Td}[Al]_{Oh}[Al]_{Oh}O_4$). The $CoFe_{0.25}Fe_{1.75}O_4$ model was established by replacing two Al^{3+} atom in $CoAl_2O_4$ unit cell with two Fe atoms. The $CoFe_2O_4$ (Supplementary Table 8) prefers inverse spinel with Co^{2+} at

octahedral sites and Fe^{3+} both at tetrahedral sites and octahedral sites ($[Fe]_{Td}[CoFe]_{Oh}O_4$).

Membrane electrode assembly (MEA) electrolyzer. A homemade MEA electrolysis cell with an anion exchange membrane was employed to evaluate the performance of the as-prepared $CoFe_{0.25}Al_{1.75}O_4$ catalyst. The cell includes two titanium end plates, on which a single serpentine flow field (area: 6.25 cm^2, 1.0 mm in width, 0.5 mm in depth, and 1.0 mm in rib) was machined. The titanium end plates were coated with a gold layer (thickness: 200 nm) to reduce the contact resistance. The $CoFe_{0.25}Al_{1.75}O_4$ was first mixed with high surface area carbon (HSAC, Ketjen black EC-600J, carbonization treatment) with a weight ratio of 1:1. The composite powder was then mixed with PTFE suspension (60 wt% PTFE dispersion in water from Chemours), isopropyl alcohol and water to prepare the anode catalyst ink. The PTFE content in the catalyst layer was controlled with 10 wt%. The catalyst ink was ultrasonicated for 30 minutes at room temperature and manually spread onto a corrosion-resistant stainless-steel mesh (SSL mesh, #500). The catalyst loading on the as-prepared electrode was 1 mg cm^{-2}. The cathode Pt electrode was fabricated with the same procedure without the addition of HSAC. A catalyst ink, consisting of commercial Pt/C catalyst (TKK, TEC10EA50E 47.1 wt% Pt, 3.22 nm in mean particle size), PTFE suspension, isopropyl alcohol and water, was manually spread onto a carbon paper (Toray 060). The catalyst loading on the electrode was 1 mg cm^{-2}. The PTFE content in the catalyst layer was 10 wt%. The IrO_2 anode was fabricated with commercial IrO_2 powder (Premetek Co) by the same procedure as for preparing the $CoFe_{0.25}Al_{1.75}O_4$ electrode. An anion exchange membrane (A901, 11 μm, Tokuyama) was employed as the membrane. To reduce the contact resistance, the membrane sandwiched by the anode electrode and cathode electrode was pressed at a pressure of 1 MPa for 5 minutes at room temperature. 0.1 M KOH was pumped into the electrode channels by a peristaltic pump at a constant flow rate of 2 ml min^{-1}. The cell temperature (60 °C) was maintained by an electric heating plate and measured by a thermocouple placed near the anode and cathode current collectors. The polarization curves were measured with an electrochemical workstation (Solartron 1470E). The water electrolysis was performed under constant current mode, in which the current was increased by 0.125 A (20 mA cm^{-2}) and retained for 5 minutes for each step until the cell voltage was reached 2.0 V. Before the water electrolysis, the as-fabricated MEA was activated by a potentiostatic mode with a scan rate of 0.5 mV s^{-1} and a terminal voltage of 2.0 V.

Data availability
The data related to this study is available from the authors upon reasonable request.

References

1. Suntivich, J., et al., A perovskite oxide optimized for oxygen evolution catalysis from molecular orbital principles. *Science* **334**, 1383-1385 (2011).

2. Grimaud, A.; Hong, W. T.; Shao-Horn, Y.; Tarascon, J. M., Anionic redox processes for electrochemical devices. *Nat. Mater.* **15**, 121 (2016).

3. Hong, W. T., et al., Toward the rational design of non-precious transition metal oxides for oxygen electrocatalysis. *Energy Environ. Sci.* **8**, 1404-1427 (2015).

4. Lee, Y., et al., Synthesis and Activities of Rutile IrO_2 and RuO_2 Nanoparticles for Oxygen Evolution in Acid and Alkaline Solutions. *J. Phys. Chem. Lett.* **3**, 399-404 (2012).

5. Chao, W., et al., Cations in Octahedral Sites: A Descriptor for Oxygen Electrocatalysis on Transition-Metal Spinels. *Adv. Mater.* **29**, 1606800 (2017).

6. Fabbri, E., et al., Dynamic surface self-reconstruction is the key of highly active perovskite nano-electrocatalysts for water splitting. *Nat. Mater.* **16**, 925-931 (2017).

7. Hsu, C.-S., et al., Valence- and element-dependent water oxidation behaviors: in situ X-ray diffraction, absorption and electrochemical impedance spectroscopies. *Phys. Chem. Chem. Phys.* **19**, 8681-8693 (2017).

8. Risch, M., et al., Structural Changes of Cobalt-Based Perovskites upon Water Oxidation Investigated by EXAFS. *J. Phys. Chem. C* **117**, 8628-8635 (2013).

9. Bergmann, A., et al., Reversible amorphization and the catalytically active state of crystalline Co_3O_4 during oxygen evolution. *Nat. Commun.* **6**, 8625 (2015).

10. Wang, H.-Y., et al., In Operando Identification of Geometrical-Site-Dependent Water Oxidation Activity of Spinel Co3O4. *J. Am. Chem. Soc.* **138**, 36-39 (2016).

11. Smith, R. D. L., et al., Spectroscopic identification of active sites for the oxygen evolution reaction on iron-cobalt oxides. *Nat. Commun.* **8**, 2022 (2017).

12. Görlin, M., et al., Tracking Catalyst Redox States and Reaction Dynamics in Ni–Fe Oxyhydroxide Oxygen Evolution Reaction Electrocatalysts: The Role of Catalyst Support and Electrolyte pH. *J. Am. Chem. Soc.* **139**, 2070-2082 (2017).

13. Zhu, Y. G., et al., Unleashing the Power and Energy of LiFePO4-Based Redox Flow Lithium Battery with a Bifunctional Redox Mediator. *J. Am. Chem. Soc.* **139**, 6286-6289 (2017).

14. Walsh, A.; Yan, Y.; Al-Jassim, M. M.; Wei, S.-H., Electronic, Energetic, and Chemical Effects of Intrinsic Defects and Fe-Doping of $CoAl_2O_4$: A DFT+U Study. *J. Phys. Chem. C* **112**, 12044-12050 (2008).

15. Terada, Y., et al., In Situ XAFS Analysis of $Li(Mn, M)_2O_4$ (M=Cr, Co, Ni) 5V Cathode Materials for Lithium-Ion Secondary Batteries. *J. Solid State Chem.* **156**, 286-291 (2001).

16. Dau, H.; Liebisch, P.; Haumann, M., X-ray absorption spectroscopy to analyze nuclear geometry and electronic structure of biological metal centers—potential and questions examined with special focus on the tetra-nuclear manganese complex of oxygenic photosynthesis. *Anal. Bioanal. Chem.* **376**, 562-583 (2003).

17. Burke, L. D.; Murphy, O. J., Cyclic voltammetry as a technique for determining the surface area of RuO_2 electrodes. *J. Electroanal. Chem.* **96**, 19-27 (1979).

18. Stoerzinger, K. A.; Qiao, L.; Biegalski, M. D.; Shao-Horn, Y., Orientation-Dependent Oxygen Evolution Activities of Rutile IrO_2 and RuO_2. *J. Phys. Chem. Lett.* **5**, 1636-1641 (2014).

19. Yeo, B. S.; Bell, A. T., Enhanced Activity of Gold-Supported Cobalt Oxide for the Electrochemical Evolution of Oxygen. *J. Am. Chem. Soc.* **133**, 5587-5593 (2011).

20. Kanan, M. W., et al., Structure and Valency of a Cobalt−Phosphate Water Oxidation Catalyst Determined by in Situ X-ray Spectroscopy. *J. Am. Chem. Soc.* **132**, 13692-13701 (2010).

21. Nkeng, P., et al., Characterization of Spinel-Type Cobalt and Nickel Oxide Thin Films by X-Ray Near Grazing Diffraction, Transmission and Reflectance Spectroscopies, and Cyclic Voltammetry. *J. Electrochem. Soc.* **142**, 1777-1783 (1995).

22. McAlpin, J. G., et al., EPR Evidence for Co(IV) Species Produced During Water Oxidation at Neutral pH. *J. Am. Chem. Soc.* **132**, 6882-6883 (2010).

23. Costentin, C.; Porter, T. R.; Saveant, J. M., How Do Pseudocapacitors Store Energy? Theoretical Analysis and Experimental Illustration. *ACS Appl. Mater. Interfaces* **9**, 8649-8658 (2017).

24. Tan, H.; Verbeeck, J.; Abakumov, A.; Van Tendeloo, G., Oxidation state and chemical shift investigation in transition metal oxides by EELS. *Ultramicroscopy* **116**, 24-33 (2012).

25. Wang, Z. L.; Bentley, J.; Evans, N. D., Valence state mapping of cobalt and manganese using near-edge fine structures. *Micron* **31**, 355-362 (2000).

26. Trześniewski, B. J., et al., In Situ Observation of Active Oxygen Species in Fe-Containing Ni-Based Oxygen Evolution Catalysts: The Effect of pH on Electrochemical Activity. *J. Am. Chem. Soc.* **137**, 15112-15121 (2015).

27. Yang, C.; Fontaine, O.; Tarascon, J. M.; Grimaud, A., Chemical Recognition of Active Oxygen Species on the Surface of Oxygen Evolution Reaction Electrocatalysts. *Angew. Chem. Int. Ed.* **56**, 8652-8656 (2017).

28. Zhang, M.; de Respinis, M.; Frei, H., Time-resolved observations of water oxidation intermediates on a cobalt oxide nanoparticle catalyst. *Nat. Chem.* **6**, 362 (2014).

29. Grimaud, A., et al., Activating lattice oxygen redox reactions in metal oxides to catalyse oxygen evolution. *Nat. Chem.* **9**, 457-465 (2017).

30. Lee, Y.-L., et al., Prediction of solid oxide fuel cell cathode activity with first-principles descriptors. *Energy Environ. Sci.* **4**, 3966-3970 (2011).

31. Mefford, J. T., et al., Water electrolysis on $La_{1-x}Sr_xCoO_{3-\delta}$ perovskite electrocatalysts. *Nat. Commun.* **7**, 11053 (2016).

32. Cheng, X., et al., Oxygen Evolution Reaction on $La_{1-x}Sr_xCoO_3$ Perovskites: A Combined Experimental and Theoretical Study of Their Structural, Electronic, and Electrochemical Properties. *Chem. Mater.* **27**, 7662-7672 (2015).

33. Grimaud, A., et al., Double perovskites as a family of highly active catalysts for oxygen evolution in alkaline solution. *Nat. Commun.* **4**, 2439 (2013).

34. Zhou, Y., et al., Superexchange Effects on Oxygen Reduction Activity of Edge-Sharing $[Co_x Mn_{1-x} O_6]$ Octahedra in Spinel Oxide. *Adv. Mater.*, 1705407 (2018).

35. Hong, W. T., et al., Charge-transfer-energy-dependent oxygen evolution reaction mechanisms for perovskite oxides. *Energy Environ. Sci.* **10**, 2190-2200 (2017).

36. Rong, X.; Parolin, J.; Kolpak, A. M., A Fundamental Relationship between Reaction Mechanism and Stability in Metal Oxide Catalysts for Oxygen Evolution. *ACS Catal.* **6**, 1153-1158 (2016).

37. Goodenough, J. B., Perspective on engineering transition-metal oxides. *Chem. Mater.* **26**, 820-829 (2013).

38. May, K. J., et al., Influence of Oxygen Evolution during Water Oxidation on the Surface of Perovskite Oxide Catalysts. *J. Phys. Chem. Lett.* **3**, 3264-3270 (2012).

39. Bajdich, M., et al., Theoretical investigation of the activity of cobalt oxides for the electrochemical oxidation of water. *J. Am. Chem. Soc.* **135**, 13521-13530 (2013).

40. Chivot, J., et al., New insight in the behaviour of $Co–H_2O$ system at 25–150°C, based on revised Pourbaix diagrams. *Corros. Sci.* **50**, 62-69 (2008).

41. Jung, S., et al., Benchmarking nanoparticulate metal oxide electrocatalysts for the alkaline water oxidation reaction. *Journal of Materials Chemistry A* **4**, 3068-3076 (2016).

42. Kim, N.-I., et al., Enhancing Activity and Stability of Cobalt Oxide Electrocatalysts for the Oxygen Evolution Reaction via Transition Metal Doping. *J. Electrochem. Soc.* **163**, F3020-F3028 (2016).

43. Newville, M., IFEFFIT : interactive XAFS analysis and FEFF fitting. *Journal of Synchrotron Radiation* **8**, 322-324 (2001).

44. Kresse, G.; Hafner, J., Ab initio. *Physical Review B* **47**, 558-561 (1993).

45. Kresse, G.; Hafner, J., Ab initio. *Physical Review B* **49**, 14251-14269 (1994).

46. Kresse, G.; Joubert, D., From ultrasoft pseudopotentials to the projector augmented-wave method. *Physical Review B* **59**, 1758-1775 (1999).

47. Perdew, J. P.; Burke, K.; Ernzerhof, M., Generalized Gradient Approximation Made Simple. *Phys. Rev. Lett.* **77**, 3865-3868 (1996).

Author contributions

T.W., S.S. A.G. and Z.X. conceived the original concept and initiated the project. T.W. prepared the materials and performed electrochemical and XRD measurements. S.S. help designed the set-up for in-situ XAS measurement. S.X. and T.W. carried out the XAS measurement. Y.D. and T.W. processed and analyzed the XAS data. J.S. worked on the DFT calculations and analysis. W.S., G.L., and B.C. carried HRTEM and STEM-EELs investigation. L.Z. conducted the measurement in MEA system. L.Z., H.W., H.L., and G.S. analyzed the MEA result. T.W. wrote the manuscript with the input from all authors, and Z.X., A.G., and S.S. revised manuscript.

Competing interests

The authors declare no competing interests.

Additional information

Supplementary information is available for this paper at